



Research paper

Cu^{II}-Na^I heteronuclear complex as anticancer entity against human breast cancer cell lines: DNA binding, cleavage, and Computational studies

Mohammad Usman^b, Sartaj Tabassum^{a,*}, Farukh Arjmand^b, Rais Ahmad Khan^c, Mohd. Sajid Ali^a, Hamad A. Al-Lohedan^a, Ali Alsalmeh^c, Mohammad Abul Farah^d, Khalid Mashay Al-Anazi^d, Musheer Ahmad^e

^a Surfactant Research Chair, Department of Chemistry, College of Sciences, King Saud University, P.O. Box 2455, Riyadh 11451, Saudi Arabia

^b Department of Chemistry, Aligarh Muslim University, Aligarh 202002, India

^c Department of Chemistry, College of Sciences, King Saud University, P.O. Box 2455, Riyadh 11451, Saudi Arabia

^d Department of Zoology, College of Sciences, King Saud University, Riyadh 11451, Saudi Arabia

^e Department of Applied Chemistry, Z.H. Engineering College, Aligarh Muslim University, Aligarh 202002, India

ARTICLE INFO

Article history:

Received 15 January 2018

Received in revised form 8 April 2018

Accepted 18 April 2018

Available online 19 April 2018

Keywords:

Cu^{II}-Na^I heterobimetallic complex

Crystal structure

DFT

Hirshfeld surface analyses

DNA cleavage activity

Cytotoxicity

ABSTRACT

Herein, we report the synthesis and structural investigation of Cu^{II}-Na^I heterobimetallic complex **1**, which comprises of the compartmental Schiff-base ligand (**H₂L**) derived from DACH (1,2-Diaminocyclohexane) and o-vanillin. B3LYP/TZVP DFT calculation was performed to get a deeper insight of the ground state electronic structure, and quantitative analysis of non-covalent interactions was carried out using Hirshfeld surface analysis to explore H-bonding, C-H...π, Cu...C-H and Cu...H-C interactions. Furthermore, *in vitro* DNA binding studies with Complex **1** demonstrated the electrostatic mode of interaction at the major groove of the DNA. Complex **1** showed the oxidative damage of pBR322 DNA via ROS generation. Additionally, *in vitro* cytotoxicity and genotoxicity of complex **1** were investigated on human breast cancer cells (MCF-7), revealed concentration-dependent cell viability at micromolar concentration level. Flow cytometric analysis confirmed the cytotoxic potential of complex **1** as the percentage of apoptotic cells were increased in the treatment group. Genotoxicity was evident in the induction of micronucleus and DNA fragmentation.

© 2018 Elsevier B.V. All rights reserved.

1. Introduction

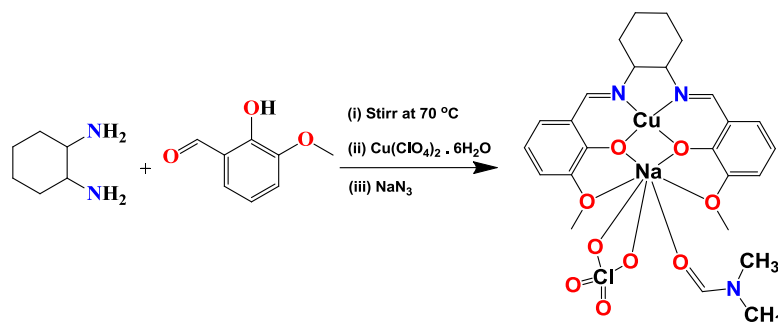
Cancer is one of the leading causes of morbidity and mortality, with approximately 14 million new cases in 2012 and 8.8 million cancer deaths globally in 2015 [1]. Altogether, nearly 1 in 6 deaths is due to cancer. According to agencies, 21.7 million new cancer cases can increase the global burden, and about 13 million cancer deaths are expected by 2030 [2]. Therefore, a major challenge for chemists is to develop new anticancer drugs with reduced toxicity and superior chemical and pharmacological properties (*viz.*, solubility, cellular uptake, kinetically stable and metabolic clearance) to increase the survival rates of patients [3]. Since Rosenberg's serendipitous discovery opened the pathway for the introduction of metal complexes in antineoplastic chemotherapy, several Pt(II) complexes (*i.e.*, cisplatin, carboplatin, and oxaliplatin) have become backbones in cancer treatment [4]. However, the

cross-resistance and severe side effects of platinum drugs have limited their clinical application, to a great extent [5]. To search for the answer of the above mentioned problems, many drug design strategies have been used, and over the last 25 years, one attractive procedure the so-called “metal-drug synergism” can be achieved by combining a pharmacologically active organic scaffold and a metal-based complex, searching for synergistic action against several pathogens, including tumor cells [6]. These chemotherapeutic agents act by inhibition of the synthesis of DNA, the primary intracellular target for several anticancer drugs. The interaction between small molecules and DNA can lead to DNA damage in cancer cells by blocking the division of cancer cells and causing cell death. Studies on the non-covalent interactions of molecules with the major groove of DNA are promising as potential new therapeutic agents [7] (See Scheme 1).

In continuation of our quest for robust design of alternative target specific metal-based anticancer agents, thus we considered new approach towards the designing of potential metallo-drugs by combining two different endogenous metal ions, copper, and

* Corresponding author.

E-mail address: tsartaj62@yahoo.com (S. Tabassum).



Scheme 1. Schematic representation of the synthesis of complex **1**.

sodium into the pharmacologically active organic scaffold that are biocompatible. Copper accumulates in tumors due to selective permeability of cancer cell membrane to copper compounds; thereby they can act as “artificial nucleases” for the sequence-specific disruption of gene function [8]. While the role of sodium during apoptosis is essential, evidence in literature has supported that sodium channels could be promising targets for cancer therapy in regards to sensitizing tumor cells to die [9]. Sodium ions induce early apoptosis and play a significant role in essential cellular functions like solute migration and differentiation, gene expression, excitation-contraction coupling and intercellular communication, etc. [10]. We have demonstrated earlier in our previous studies that heterobimetallic complexes of the copper exhibit a remarkable antiproliferative profile and show preferential selectivity inside the cells, inducing apoptosis. The strategic design and synthesis of heteronuclear complexes are quite challenging. The metal centers in heteronuclear systems promote cooperative synergic interactions, for example in biological systems, cooperative interactions are commonly observed which accomplish an extraordinary range of catalytic transformations [11].

Complex **1** structure was elucidated by single crystal X-ray diffraction and other spectroscopic techniques. Although there are a few literature reports of heteronuclear complexes incorporating sodium and copper, the aqua-soluble Cu/Na heteronuclear complex examples remain very scant [12]. The binding affinity towards DNA has been studied by using absorption, emission spectroscopy, and DNA electrophoresis. The anti-cancer potential of complex **1** was evaluated in human breast adenocarcinoma MCF-7 cells through cytotoxicity, apoptosis and DNA damage assays.

2. Experimental section

2.1. Materials

$\text{Cu}(\text{ClO}_4)_2 \cdot 6\text{H}_2\text{O}$ (Sigma-Aldrich), *o*-vanillin (Sigma-Aldrich), 1,2-Diaminocyclohexane (Alfa Aesar) and calf thymus DNA (CT DNA) (Sigma-Aldrich), pBR322 DNA (Genei) used as received. From Invitrogen (Carlsbad, CA, USA), FBS (Fetal bovine serum), penicillin-streptomycin and trypsin/ EDTA were obtained. PBS (phosphate buffered saline), dimethyl sulfoxide (DMSO), ethidium bromide, acridine orange, Trypan blue, Cytochalasin-B, agarose for electrophoresis and Dulbecco's Modified Eagle's medium (DMEM), were obtained from Sigma-Aldrich (St Louis, MO, USA). The Cell Titer 96[®] (Non-radioactive Cell Proliferation Assay kit), purchased from Promega (Madison, WI, USA). All the culture wares and consumables used in these experiments were from Nunc, Denmark.

2.2. Methods and instrumentation

Instruments used for Microanalysis was CE-440 elemental analyzers (Exeter Analytical Inc.), FT-IR was carried out on

Perkin-Elmer Model 1320 spectrometer (KBr disk, 400–4000 cm^{-1}), Perkin-Elmer UV-vis spectrophotometer, Shimadzu RF-5301 PC spectrofluorophotometer. Axygen horizontal electrophoretic assembly with power supply and Vilber-Infinity gel documentation system for imaging.

2.3. Synthesis of $[\text{Cu}^{\text{II}}\text{Na}^{\text{I}}\text{L}(\text{DMF})(\text{ClO}_4)]$ (**1**)

A solution of *o*-vanillin (2 mmol, 10 mL MeOH) was mixed with DACH (2 mmol, 0.24 mL). The mixture was allowed to stirring at 70 °C for a period of 3 h to give deep yellow clear solution. A methanolic solution of $\text{Cu}(\text{ClO}_4)_2 \cdot 6\text{H}_2\text{O}$ (0.37 g, 1 mmol) was added to the above reaction mixture which was refluxed with constant stirring for 2 h. After this was added, sodium azide (1 mmol, 65 mg) in a methanol-DMF (1:2) mixture (15 mL) to above reaction mixture and stirred for 2 h. After 2–3 weeks crystals suitable for X-ray were obtained on slow evaporation in a refrigerator of brown color.

Yield 88%, M.P. 210 °C. Anal. Calc. for $[\text{C}_{25}\text{H}_{31}\text{ClCuNaO}_9]$ (%): C, 46.95; H, 4.89; N, 6.57; Found: C, 46.84; H, 4.78; N, 6.51.

2.4. Single crystal X-ray crystallography

To obtain crystallographic data of complex **1**, Bruker SMART APEX CCD diffractometer at 100 K on a using graphite monochromatic MoK_α radiation ($\lambda = 0.71073 \text{ \AA}$) [13–17] (for details see SI). The refinement and crystal data are presented in Table 1. Selective bond distances and angles are given in Tables S1 and S2.

2.5. Theoretical calculations

The ORCA 3.0.1 programmed was used for theoretical calculations [18]. The quantum chemical calculations were performed by applying the DFT method with Becke-3-Lee-Yang-Parr (B3LYP) supplemented with the balanced polarized triple-zeta def2-TZVP basis set for all atoms [19]. The initial coordinates was taken from the single crystal X-ray structural data. The resolution of identity approximation with decontracted auxiliary def2-TZV/J coulomb fitting basis set and the chain-of-spheres approximation were subjected, to fasten the calculations [20]. The Crystal Explorer software was used for mapping the Hirshfeld surface by taking crystal structure data from .cif file [21].

AutoDock Vina software package was utilized for the molecular docking studies [22]. The Pre-docking preparation of the ligand (complex **1**) and receptor (DNA: PDB; 1BNA) was done by MGL Tool-1.5.6. Discovery Studio 4.1 and Pymol molecular graphic visualization programs were used for the imagining of most favorable docked poses [23].

Table 1
Crystal and Structure Refinement Data for complex **1**.

Parameters	Complex 1
Formula	C ₂₅ H ₃₁ ClCuN ₃ NaO ₉
Fw (g mol ⁻¹)	639.51
Crystal System	Monoclinic
Space Group	P2 ₁ /c
a (Å)	14.0488(15)
b (Å)	12.2202(13)
c (Å)	16.4625(16)
β(deg)	94.492(2)
U (Å ³)	2817.6(5)
Z	4
ρ _{calc} (g/cm ³)	1.508
μ (mm ⁻¹)	0.942
F(0 0 0)	1324
Crystal size (mm)	0.28 × 0.20 × 0.15
Temp (K)	296(2)
Measured reflns	19,046
Unique reflns	3998
GOF ^a	1.030
Final R ^b indices	R1 = 0.0482
[I > 2σ(I)]	wR2 = 0.1297
R ^b indices(all data)	R1 = 0.0622
	wR2 = 0.1409
CCDC	1,532,654

^a GOF is defined as $\{\sum[w(F_0^2 - F_c^2)]/(n - p)\}^{1/2}$ where n is the number of data and p is the number of parameters. ^bR = $\{\sum\|F_0 - |F_c|\}\} / \{\sum w(F_0^2 - F_c^2) / \sum w(F_0^2)\}^{1/2}$

2.6. DNA binding and cleavage experiments

The DNA binding and cleavage experiments were carried out by using standard protocol with slight modification made by us (for detail see ESI). [24,25]

2.7. Cell cultures

MCF breast cancer cell line was obtained from ATCC, Rockville, USA. The MCF cells were maintained under standard conditions in DMEM along with PBS (10%) and antibiotics (1% penicillin/streptomycin (for detail see ESI).

2.8. Cytotoxicity assay

The colorimetric MTT (3-(4,5-dimethylthiazol-2-yl)-2,5-diphenyltetrazolium bromide) Assay was carried out with slight modification to study the cytotoxicity of the complex **1** against MCF7 human breast cancer cells. (for detail see ESI).

2.9. Morphological changes analysis

To observe morphological changes in cells (MCF-7) induced upon treatment with complex **1** for 24 h are visualized under 100X a phase contrast inverted microscope (for detail see ESI).

2.10. Detection of apoptosis by flow cytometry

The Apoptosis of the cells was examined in MCF-7 cells by Annexin V-Propidium Iodide (PI) double staining method using the annexin V-FITC apoptosis detection kit (BD Biosciences, San Diego, USA). Briefly, 1×10^5 cells/mL were grown for overnight and exposed to complex **1** (2.5 and 5.0 μM) in 6-well plates for 24 h. At the end of the exposure, cells were washed with cold PBS, trypsinized and centrifuged at 1000 rpm; the cell pellet was rewashed with PBS and re-suspended in 100 μL of 1X binding buffer (1×10^6 cells/mL). Then, annexin V-FITC and PI, 5 μL each was

added to the cell suspension, and the cells were gently vortexed. Then, the cells were incubated for 20 min at room temperature (25 °C) in the dark. Then, the samples were diluted by adding 400 μL 1X binding buffer. Annexin-V/ PI fluorescence was studied on BD FACSCalibur flow cytometer for the samples. By the help of Cell Quest Pro software (BD Biosciences), samples data was analyzed and approximately 10,000 events were acquired in a total/sample

2.11. Cytokinesis-block micronucleus (CBMN) assay

The CBMN assay was carried out using the protocol described by Fenech, (2007). Briefly, the MCF-7 cells were seeded in Lab-Tek-II chamber slides (Nunc, Denmark) at a density of (1×10^5 cells/ml). Then cells were exposed to different concentrations of complex **1** (2.5 and 5.0 μM) for 24 h. At the end of treatment, the culture medium was removed, and cells were washed twice with PBS and cytochalasin-B at a final concentration of 4 μg/mL (dissolved in fresh medium) was added to the cells, and cultured the cells for another 24 h to block the cytokinesis after mitosis. Then, PBS has been used to wash the cells and fixed in fresh and cold fixative solution (MeOH: CH₃COOH, 3:1, v/v) for 20 min at room temperature. The cells were stained with acridine orange (125 μg/mL in phosphate buffer, pH 7.4). The chambers were removed, and slides were observed at 400× magnification under a compound microscope (Olympus BX41, Japan) equipped with fluorescence unit accompanied with digital camera. The micronucleus frequency was determined for 1000 binucleated MCF-7 cells (BNCs) in each treatment and control group.

2.12. Detection of DNA fragmentation by agarose gel electrophoresis

Apoptotic DNA fragmentation was analyzed by using Apoptosis DNA ladder kit (Roche Diagnostics, Mannheim, Germany). Briefly, 1×10^5 cells/ml were grown for overnight and exposed to complex **1** (2.5 and 5.0 μM) in 6-well plates for 24 h. The manufacturer's protocol was employed to extract DNA. The quantity and purity of extracted DNA were checked by measuring optical density (OD) in a Nanodrop UV-spectrophotometer (Thermo Fisher Scientific, USA). For DNA ladder analysis, an equal amount of DNA (1 μg) and 100 bp DNA ladder marker was loaded and run on a 1.0% agarose gel containing 20 μg/mL ethidium bromide at 90 V, and the DNA fragments were visualized by exposing the gel to UV light and images were captured in a gel-doc system (Bio-Rad, USA).

2.13. Statistical analysis

All the experiments were carried out in triplicate. The values obtained are ±standard error of the mean (SEM). The Student's *t*-test was applied at a level of significance of $P < 0.05$.

3. Results and discussion

The DACH and o-vanillin in 1:1 M ratio, condensation reaction *in situ* resulted in the formation of ligand (H₂L) (deep yellow) and successively its Heterobimetallic Cu^{II}-Na^I salen complex [CuL₁Na(DMF)(ClO₄)] (**1**) was synthesized. The complex **1** was characterized using %CHN, FTIR, UV-vis, and single X-ray crystallography. The complex is quite stable in air and soluble in H₂O, MeOH, DMF, MeCN, and DMSO. Complex **1** was pre-designed to endorse its recognition with DNA helix at a specific point. In the present study, we observed elevated annexin V binding to phosphatidylserine at the cell membrane through flow cytometric apoptosis assay. The clastogenic mode of action for complex **1**

was confirmed by micronucleus induction in MCF-7 cells that resulted from DNA damage during anaphase nuclear division.

3.1. Structure description

Heterobimetallic Cu^{II}-Na^I salen complex [Cu^{II}Na^I(DMF)(ClO₄)] (**1**) was structurally described by the help of X-ray crystallography. The crystallographic data and refinement parameters details are briefly presented in Table 1. Some of the important bond angles and bond distances are also listed in Tables S1 and S2 (see ESI).

Single-crystal X-ray structural study revealed that complex **1** crystallized in the monoclinic *P*21/*c* space group with *a* = 14.0488 (15) Å, *b* = 12.2202(13) Å, *c* = 16.4625(16) Å, β = 94.492° (2) per unit cell lattice parameters. Fig. 1 exhibited the asymmetric unit for [[CuL₁Na(DMF)(ClO₄)] (**1**) comprises of Cu(II) metal ion bonded to a tetra-dentate di-anionic ligand (L²⁻), i.e., -NNOO- donor. This Cu(II) center with four coordination sites displayed a square-planar geometry, [Cu1-N1 1.929(3) Å; Cu1-N2 1.921(3) Å; Cu1-O1 1.876 (2) Å and Cu1-O2 1.892(2) Å] from the deprotonated Schiff base ligand (L²⁻). Thus, the arrangement around the central metal Cu (II) is slightly distorted square-planar arrangement. The sodium ion is located in open compartment, being surrounded by seven oxygen atoms: two phenolate and two methoxy oxygen atoms arising from the Schiff base [Na1-O1 2.348(2) Å; Na1-O2 2.330 (3) Å; Na1-O3 2.721(3) Å; Na1-O4 2.664(3) Å;] and two oxygen atoms from the bidentate perchlorate ions [Na1-O6 2.537(4) Å; Na1-O8 2.545(4) Å] and one from the DMF moiety [Na1-O9 2.321(4) Å]. All the observed Cu–N, Cu–O, and Na–O bond distances are within the range of the previously reported heterobimetallic Cu^{II}-Na^I complexes [26].

At the supramolecular level, the heterobimetallic units interact through hydrogen bonds (C–H...O) established between the oxygen atom of the coordinated perchlorate ligand (O5) and the hydrogen atom (H7) of the L²⁻ ligand with the symmetry related (-*x*, -1/2 + *y*, 1/2 - *z*) belonging to a neighboring molecular unit, resulting in a supramolecular Zig-Zag 1D-chain (Fig. S1). Further,

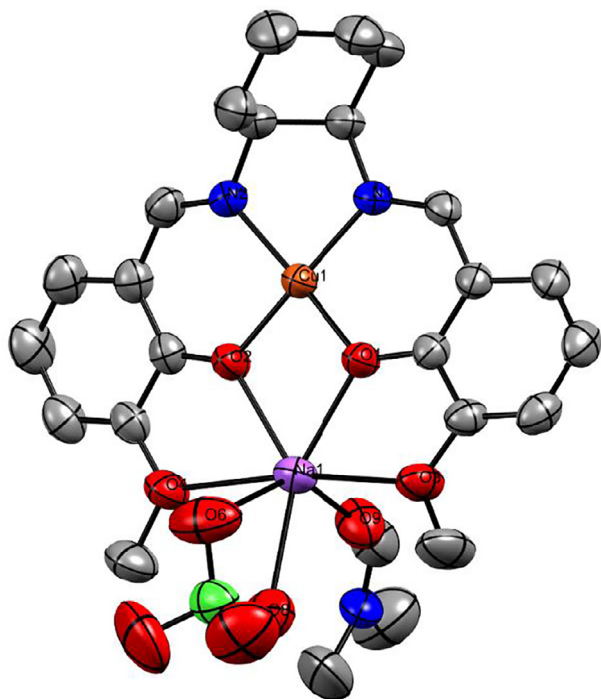


Fig. 1. The structure of the complex **1** is presented in thermal ellipsoids with 50% probability.

these Zig-Zag 1D-chains again communicated to each other and form inter-chain hydrogen bond (C–H24...O9) with the symmetry (1-*x*, 1-*y*, -*z*) to generate a Kagome-type 2D-supramolecular sheet (Fig. S2).

3.2. Spectral characterization

The distinct band at 1626 cm⁻¹ due to the azo-methine (C=N) group are noticed in the IR spectra of complex **1** (Fig. S3) [27]. Another band at 1080 cm⁻¹ indicates the presence of coordinated perchlorate moiety. The band in the range 2928–2935 cm⁻¹ are due to C–H stretching vibrations.²⁷ Moreover, a sharp and strong band is observed at 1244 cm⁻¹, indicative of aliphatic C–N stretching vibrations.

The electronic spectrum of complex **1** was observed in methanolic solution which give rise to two prominent absorption signals at 231 nm and 277 nm corresponding to π–π* intraligand transition. However a broad absorption maximum at 368 nm was ascribed for LMCT transition (see ESI, Fig. S4). A single absorption band at 534 nm are consistent with the observed square-based geometry around the Cu(II) center [27].

The ESI-MS spectrum of complex **1** exhibited a fragmentation peak at *m/z* 467 was observed for [C₂₂H₂₄CuN₂NaO₄ + H⁺] which gives evidence of the formation of the heterobimetallic complex **1** (Fig. S5).

The emission spectrum of complex **1** are studied in methanolic solution at 25 °C, exhibits fluorescence at 325 nm when it is being excited at 277 nm, whereas a weak signal appeared at 445 nm upon excitation at 368 nm (see ESI, Fig. S6). This band may be attributed to the intra-ligand charge transfer (ILCT) or ligand-ligand charge transfer (LLCT) or both of them.

The stability of the complex **1** in solution phase (tris-HCl buffer at pH = 7.4) was studied at various times till 48 h using UV-vis spectrophotometer (Fig. S7). The recorded UV-Vis spectra doesn't exhibits any considerable intensity or positional changes in the absorption bands indicating their stability under experimental conditions.

3.3. Hirshfeld surface analyses

The Hirshfeld surfaces mapped with *d*_{norm} range of -0.5–1.5 Å, shape index (-1.0–1.0 Å) and curvedness (-4.0–0.4 Å) for complex **1** were illustrated in Fig. 2. The *d*_{norm} surface displayed a red-white-blue color arrangement. The deep red spots show shorter contacts e.g. hydrogen bonding. The white areas correspond to contacts around the van der Waals separation like H...H, and the blue regions are devoid of such close contacts. The dominant interaction between O...H, C...H and H...N atoms can be seen in the Hirshfeld surface as the bright red areas in *d*_{norm} surface. Other visible spots in the *d*_{norm} surface correspond to H...H. The small extent of area and light color on the *d*_{norm} surface indicates weaker and longer interactions other than hydrogen bonds. In the shape index surface red regions corresponding to C–H...π interactions and 'bow-tie patterns' indicated the presence of aromatic stacking (π...π) interactions. The curvedness surface specified the electron density of surface curves around the molecular contacts

The 2D-fingerprint plots of complex **1** are presented in Fig. 3, counterpart to above described surfaces which quantitatively summarized the nature and type of intermolecular contacts experienced by the molecules in the crystal. The fingerprint plots can be decomposed to highlight particular atom pair close contacts. This decomposition enables parting of contributions from different interaction types, which overlap in the full fingerprint. The amount of H...H, C...H and C...C interactions covers 47%, 18.6% and 1.9% of the total Hirshfeld surface for complex **1**. Moreover, O...H, H...N,

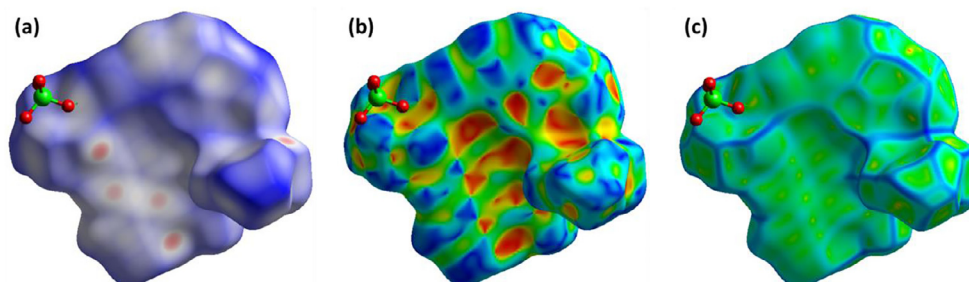


Fig. 2. Hirshfeld surfaces mapped with d_{norm} (left), shape index (middle) and curvedness (right) for complex **1**.

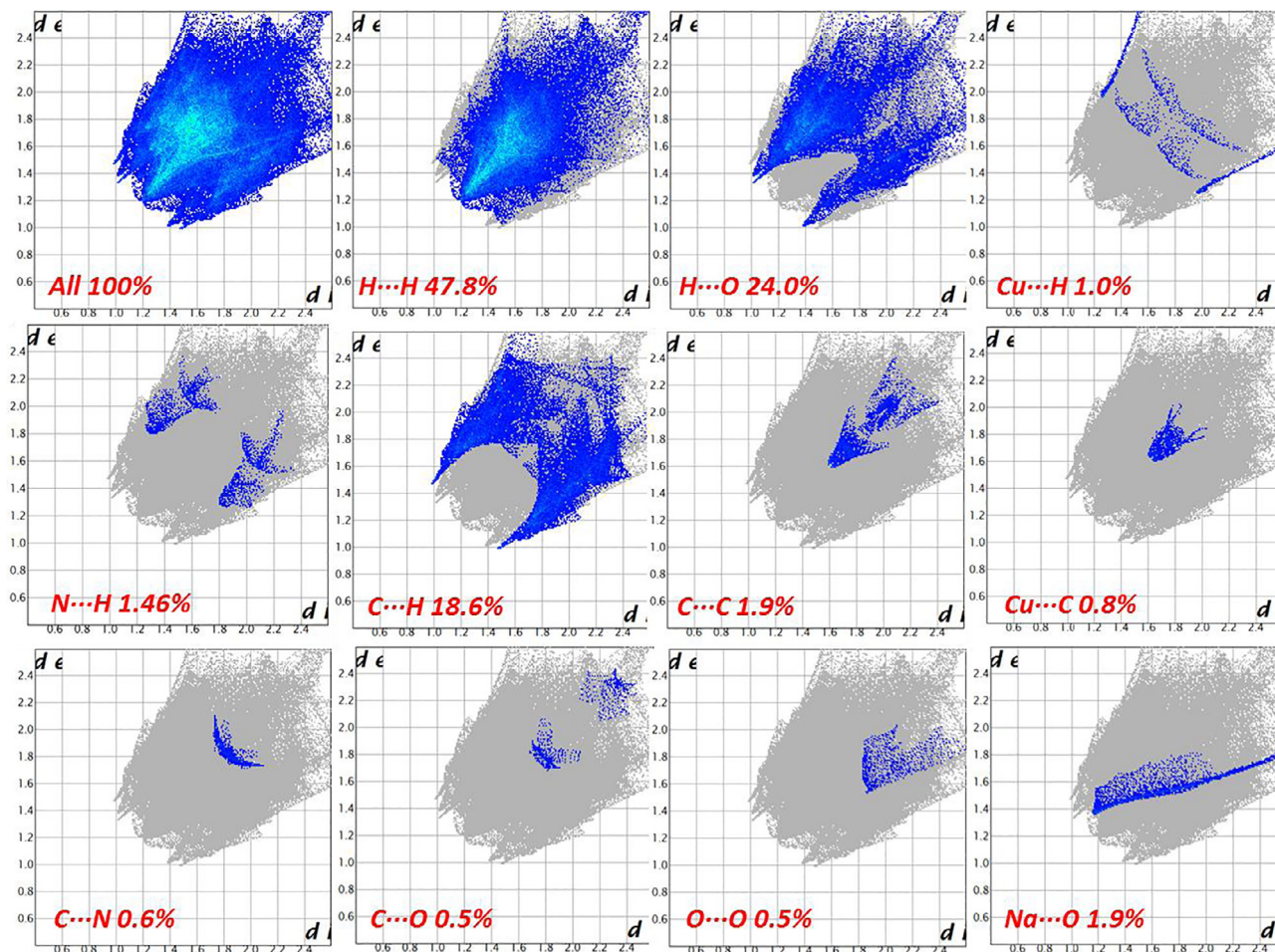


Fig. 3. The 2D fingerprint plots of interatomic interactions for complex **1** showing the percentages of contacts contributed to the total Hirshfeld surface area of the molecules.

and C–H...Cu interactions comprise 24.0%, 1.46%, and 1% of the total Hirshfeld surface for complex **1**, respectively.

3.4. DNA binding and cleavage studies

The absorption bands of the complex **1** originating in the regions 231, 277 and 368 nm are attributed to interligand transitions and LMCT, respectively. The equilibrium binding constant (K_b) of the complex **1** to CT-DNA was determined by UV-vis titration experiments. On addition of CT-DNA to the complex solution, the UV-vis absorption bands in the regions 231 and 277 nm showed a hyperchromism with a blue shift of 2–8 nm (see ESI, Fig. S8) for complex **1**. The hyperchromic shift due to the interligand transition for complex **1** was taken to calculate the binding affinity of

complex **1** with CT-DNA. The resulting hyperchromicity of complex **1** in the interligand transition band is possibly due to outersphere contact with DNA via an electrostatic mode of interaction [28]. This kind of binding may lead to an apparent modification in the conformation of DNA expected the cleavage of its secondary structure. Further, the binding strength of complex **1** towards the CT-DNA was found to be $(2.05 \pm 0.11) \times 10^4 \text{ M}^{-1}$.

In the fluorescence spectra, a significant emission intensity at ca.330 nm was exhibited by the complex **1**, upon excitation with a wavelength of 277 nm light (λ_{ex}). Further enrichment in the fluorescence intensity was perceived upon concomitant adding CT-DNA ($0\text{--}1.8 \times 10^{-4} \text{ M}$) with no significant shift, (see ESI, Fig. S9). The increase of emission intensity demonstrated that complex **1** interacts with DNA and can be efficiently protected into the

interior hydrophobic environment of the DNA helix, which can inhibit quenching and increases the fluorescence intensity of the complex **1** when binds to it. Accordingly, the binding of complex **1** to DNA, restricted the complex flexibility at the binding cavity owing to the inaccessibility of the solvent water molecules to enter the hydrophobic environment inside the DNA helix, contributing to a reduction in the vibrational mode of relaxation and therefore vanishing the quenching effect of solvent molecules. Furthermore, the binding strength of complex **1** with CT-DNA was determined by calculating binding constant (K) value with the help of the Scatchard equation [24d] which were found to be $(1.90 \pm 0.15) \times 10^4 \text{ M}^{-1}$.

Upon addition of increasing concentration of complex **1** to DNA-EB adduct ($[\text{DNA}]/[\text{EB}] = 1$) solution, the emission signal at 596 nm displayed quenching up to 70% fluorescence intensity, upon varying the molar ratio of the complex to DNA ($r = [\text{complex}]/[\text{DNA}]$) from 1.6 to 15.0 (see ESI, Fig. S10). The quenching of DNA-EB fluorescence infers the displacement of the EB molecule by complex **1** from their DNA-EB adduct. However, the displacement of the EB was not 100%, therefore partial intercalation as well as the electrostatic binding of the complex **1** are possible [29]. The quenching efficiency (K_{sv}) was calculated, and the quenching parameters are in close proximity with the Stern-Volmer equation,

$$I_0/I = 1 + K_{sv}[Q]$$

where, I_0 and I are the fluorescence intensities without and with the complex **1**(quencher), respectively. K_q quenching constant (Stern-Volmer constant) and Q is the concentration of the complex **1** (quencher). The slope of the plot of I_0/I versus $[Q]$ gave K_{sv} value of $(1.25 \pm 0.17) \times 10^4 \text{ M}^{-1}$ for complex **1**, indicating the strong affinity to DNA.

To assess the nuclease activity of the complex **1** against pBR322 DNA as substrate in 5 mM Tris-HCl/50 mM NaCl, pH = 7.4 buffer. A pBR322 DNA is characterized by showing the supercoiled (SC), the open circular (OC), and the linear (L) forms. Differences in electrophoretic mobility of any of the mentioned forms are generally drawn as evidence of direct metal-DNA interactions. In Fig. 4, the gel electrophoretic observed, the mobility of pBR322 DNA changes when complex **1**/pBR322 DNA proportion increases due to the conversion of SC from to OC form of pBR322 DNA. With the increase in complex **1**/pBR322 DNA proportion, the amount of SC form gradually diminished with the appearance of OC form (Lane 2–6). However, at a concentration of 10 μM of complex **1** displayed potent DNA nuclease activity, significant conversion of SC into OC was observed, without the presence of LC (Lane 2–6) suggestive of single-strand cleavage [27].

To analyze the mechanism of action of complex **1** for its potential nucleolytic activity and generation of type of ROS, the electrophoretic pattern was studied in the presence of standard radical scavengers Fig. 4b, (lane 6 and 7) it was observed that DNA cleavage was inhibited significantly in the presence of NaN_3 and SOD, con-

firms singlet oxygen as well as superoxide anion are responsible species for cleavage. However, presence of DMSO and alcohol does not significantly quenches cleavage of DNA (lane 8 and 9) ascertains that freely diffusible hydroxyl radical was not involved in the cleavage process (Lane 8 and 9). Since, complex **1** was able to cleave DNA in the absence of any reducing agent, which implies that DNA might be cleaved by oxidative pathway [30].

Moreover, to ascertain the binding propensity of the complex **1** with DNA, the reaction in the presence of DAPI (a minor groove binder) and Methyl Green (a major groove binder) were carried out (Lane 10 and 11). No deceptive inhibition was noticed in presence of DAPI whereas in the presence of MG significant inhibition was observed. Thus it implicates the major groove binding affinity of the complex **1** towards pBR322 DNA. The above findings corroborates well with molecular docking studies.

3.5. Density functional theory

The HOMO-LUMO energy gap play a significant role in the analysis of chemical properties e.g. reactivity, kinetic stability and electrical transport. The electrons of outer most orbitals are taking part in the building HOMOs and behave as an electron donor while in most low energy empty orbitals which behave as an electron acceptor. This HOMO-LUMO energy gap considered as a quantum mechanical descriptor (QM) in creating a correlation between molecular activity and structure for many chemical and biochemical systems. Lately, this QM descriptor has also been applied to explore the bioactivity from the intermolecular transfer of charge which correlated with many biological activities e.g. DNA binding strength, antibacterial and antioxidant [31]. The intra-molecular charge transfer (ICT) from electron rich groups to electron deficient groups via π -conjugated path is facilitated by small HOMO-LUMO energy gap whereas the stability and low reactivity of molecules related to the large HOMO-LUMO energy gap [32a]. For complex **1**, HOMO-LUMO energy gap was calculated 3.44 eV (Fig. 5).

In the complex **1**, significant part of LUMO and LUMO + 1 was centered on Schiff base donor atoms and o-vanillin moiety along with a significant amount on copper ion, while LUMO + 2 mainly delocalized in between the Cu(II) and Na(I) and LUMO + 3 was centered on dimethylformide (DMF) and some part on o-vanillin moiety of the Schiff base ligand coordinated to Na(I). The lower LUMO energy of the interacting molecule to the DNA results greater DNA binding strength. N. Kurita et. al. revealed that HOMO and HOMO-1 of DNA were occupied on base pairs and HOMO - x ($x = 2-3$) on phosphate backbone [32b]. Hence, on interaction with DNA lower E_{LUMO} of complex **1** provides accommodation for an incoming electronic charge from HOMO of the DNA base pairs. Therefore, transfer of charge density from HOMO, HOMO-2, and HOMO-3 of DNA to LUMO, LUMO + 1, LUMO + 2, and LUMO + 3 of complex **1**, occurred.

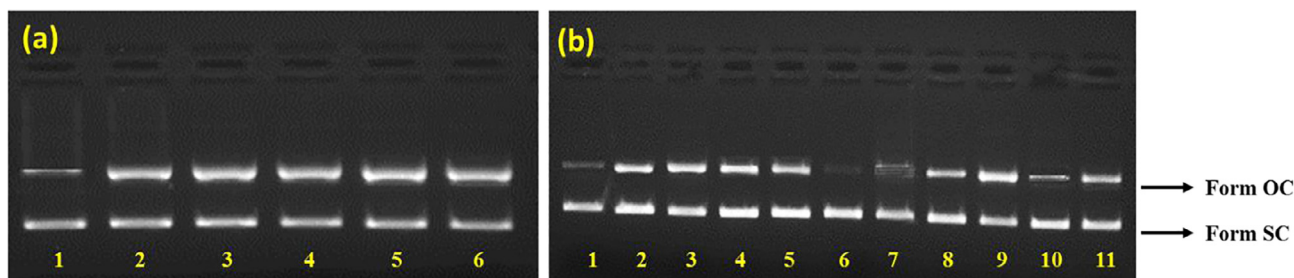


Fig. 4. (a) The electrophoretic patterns depicting the concentration dependent cleavage: lane 1: control, lane 2–6 (increasing concentration of DNA from 5 to 25 μM) (b) (i) Mechanistic pathway for the cleavage: Lane 1, DNA control; Lane 2, DNA + **1** + Asc; Lane 3, DNA + **1** + H_2O_2 ; Lane 4, DNA + **1** + GSH; Lane 5, DNA + **1** + MPA; Lane 6, DNA + **1** + NaN_3 ; Lane 7, DNA + **1** + SOD; Lane 8, DNA + **1** + DMSO; Lane 9, DNA + **1** + tBuOH; (ii) Groove binding affinity: Lane 10, DNA + **1** + MG; Lane 11, DNA + **1** + DAPI.

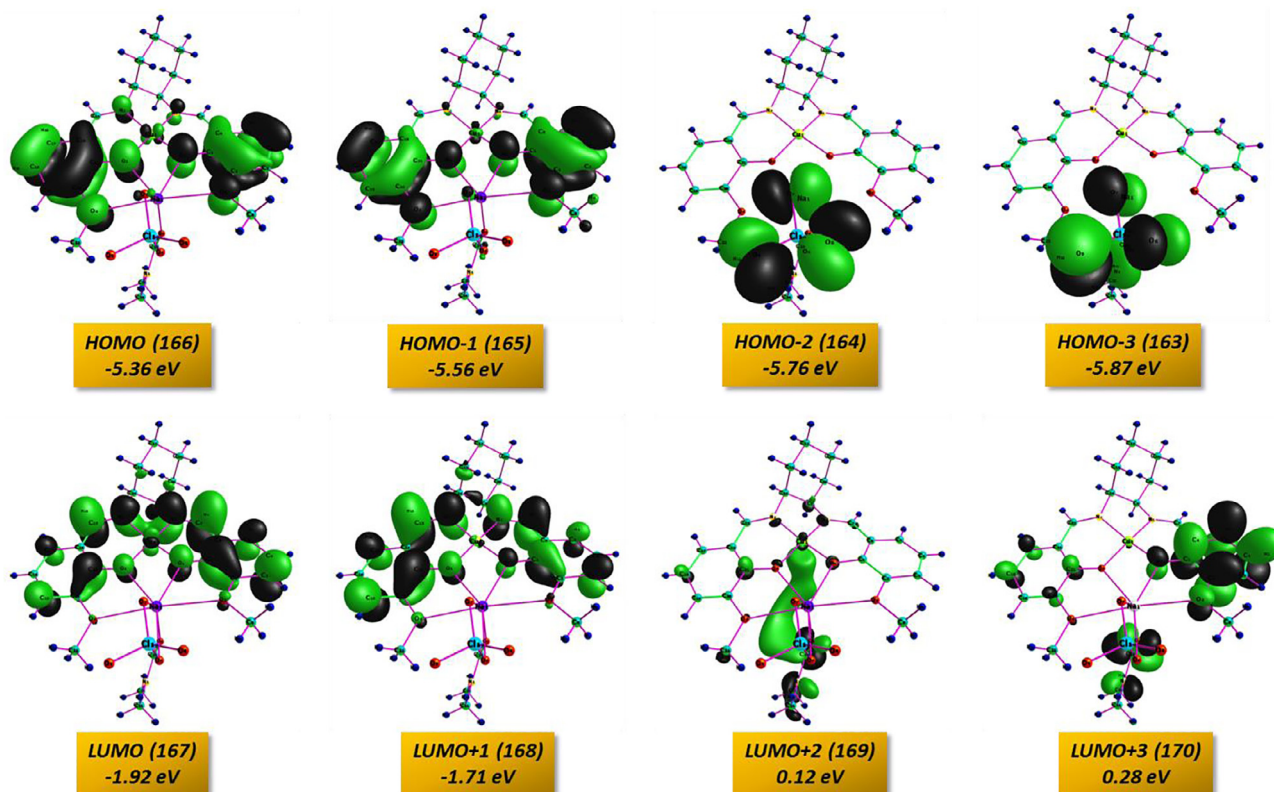


Fig. 5. The Diagrammatic representation of complex **1** showing Frontier Molecular Orbitals.

3.6. Molecular docking

Since the complex **1** possesses significantly good DNA binding propensity and nuclease activity, the molecular docking study have been carried out to examine the favorable binding site of heterodinuclear Cu-Na salen complex to DNA helix. Moreover, molecular docking investigations give visual illustration of the promising binding mode and site of interaction of the potential drug candidate with their target biological molecule [33]. The resulting binding affinity determined for the minimum energy favorable docked pose of complex **1** with the DNA target was found to be -8.32 kcal/mol which showed that complex **1** interacts with DNA

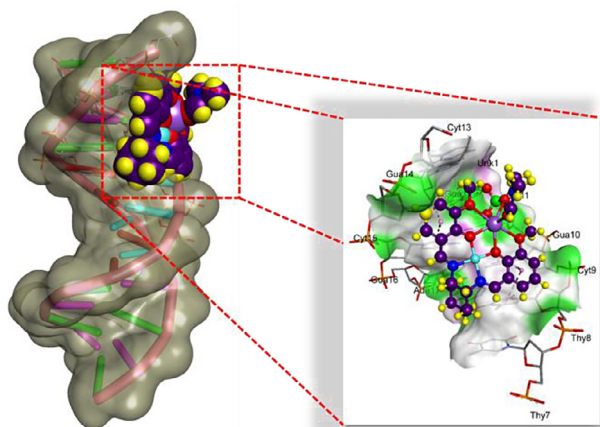


Fig. 6. The Molecular docked model of complex **1** with the major groove of DNA.

Table 2

Non-covalent interactions of the complex **1** with DNA.

Name	Distance (Å)	Category	Type
1: O7 - A: DG10: N7	2.53	Hydrogen Bond	C-Hydrogen Bond
1: O5 - B: DG14: O6	2.75	Hydrogen Bond	C-Hydrogen Bond
1: H22A - B: DG14: N7	3	Hydrogen Bond	C-Hydrogen Bond
A: DC9: C5 - 1	3.62	Hydrophobic	π - σ
A:DT8 - 1	4.55	Hydrophobic	π - π , T-shaped
A: DC9 - 1	4.98	Hydrophobic	π - π , T-shaped
B: DG14 - 1	4.3	Hydrophobic	π - π , T-shaped
B: DC15 - 1	5.51	Hydrophobic	π - π , T-shaped

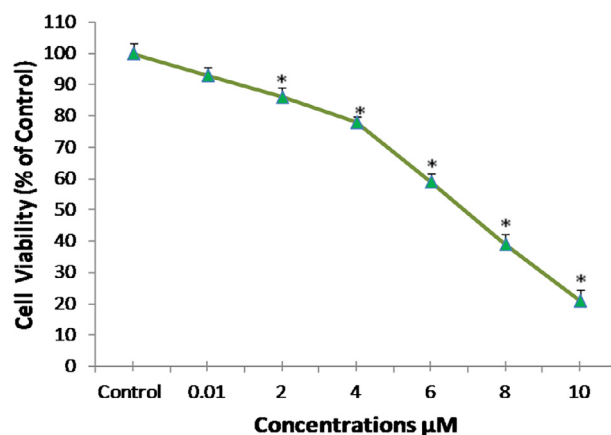


Fig. 7. Cytotoxicity of complex **1** against MCF-7 cells upon treatment with indicated concentrations for 24 h and analyzed by MTT assay. Data is reported as \pm SE.* Significant ($p < 0.05$).

through an electrostatic mode including an inside edge hydrogen bonding contacts with the oxygen and nitrogen atoms of the guanine base or fitted best into the curve counter of major groove of DNA in the slim and to some extent deeper G–C region of the major groove in vicinity of G-10, G-14, C-9, C-15 and T-8 DNA base pairs (Fig. 6). While o-vanillin moiety of Schiff base ligand scaffold planarity is more compatible to forming π - π stacking exchanges, which gives a partial match of complex **1** inside the DNA strand. A detailed description of formed non-covalent interactions which stabilized the complex **1**-DNA aggregate is given in Table 2.

3.7. Cytotoxicity on MCF-7 cell

To study the cytotoxicity of complex **1** in MCF-7 cells, MTT assay was performed. Fig. 7 displays the percent cells viability exposed to different concentrations of **1** (0.1–10 μ M). The IC_{50} value observed at 24 h after the treatment of MCF-7 with complex **1** is found to be 6.75 μ M which is significantly good in comparison to positive control cisplatin (IC_{50} = 5.40 μ M) and doxorubicin (IC_{50} = 12.01 μ M, a standard drug) and the ligand (IC_{50} = 21.30 μ M). The fall in the cell viability was detected significant ($p < 0.05$) which

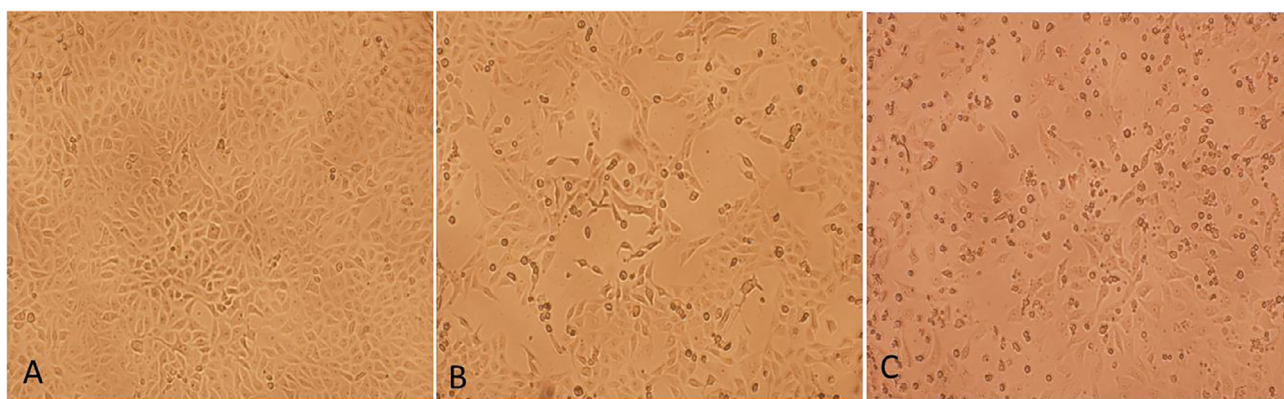


Fig. 8. Morphological changes analysis of MCF-7 cells by phase contrast inverted microscopy. (A) Control (B) complex **1** (2.5 μ M) (C) complex **1** (5.0 μ M), Magnification: 100X.

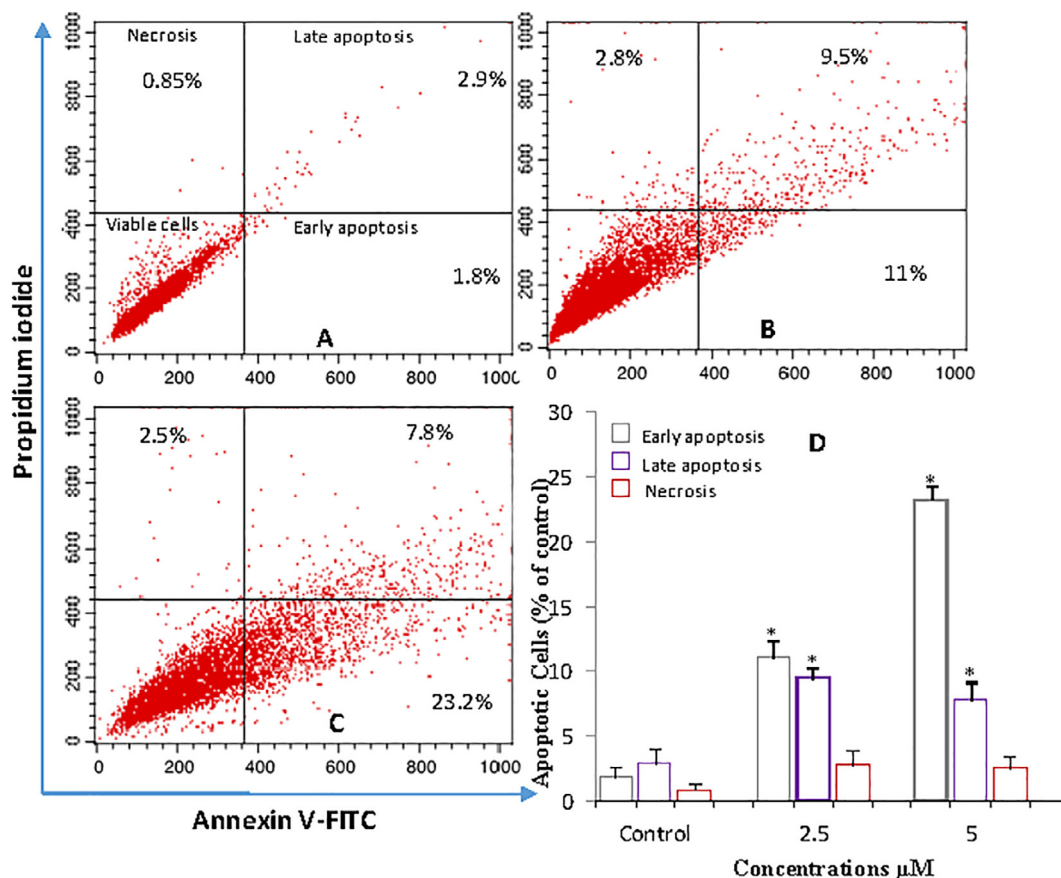


Fig. 9. Flow cytometric analysis (annexin V-FITC/PI assay) of MCF-7 cells exposed to indicated concentrations of complex **1** including an untreated control for 24 h. Representative dot plots showing the viable cells (%), early apoptosis (%), late apoptosis (%) and necrotic cells (%) (A) Control, (B) Complex **1** (2.5 μ M) (C) Complex **1** (5.0 μ M). (D) Bar diagrams are showing the percentage of apoptosis observed by flow cytometric analysis of MCF-7 cells. Data presented in \pm SE. * Significant ($p < 0.05$) compared with controls.

was also concentration dependent. At the highest concentration of 10 μM cell proliferation was reduced to 79% while at the lower concentration of 0.1 μM 93% cell growth was registered.

3.8. Morphological changes analysis

To evaluate the cytotoxicity at the morphological level, cells were treated with two concentrations of complex **1** (2.5 and 5.0 μM) below IC_{50} value for 24 h. Fig. 8, depicts the representative image observed morphological changes of MCF7 cells. In control, the morphology was undisturbed (Fig. 8A) with normal shape, attached with the surface and 95–100% confluence was noticed. Conversely, in the treated groups the cells lost their normal epithelial cell morphology, becoming longer, and swelled. A decreased cell density was witnessed upon treatment with complex **1** of MCF-7 cells (Fig. 8B, C). More detached and round cells were observed at a higher concentration of 5.0 μM .

3.9. Detection of apoptosis by flow cytometry

Using flow cytometry, the percentages of apoptotic and necrotic cells via double staining with Annexin V and PI were analyzed. The

positioning of quadrants on dot plots was labelled, and displayed living cells (Annexin V–/PI–), early apoptotic cells (Annexin V+/PI–), late apoptotic cells (Annexin V+/PI+), and necrotic cells (Annexin V–/PI+). Representative results were presented in Fig. 9. These data demonstrate that incubation of MCF-7 cells with complex **1** reduces the number of the viable cells and apoptotic cells increases. However, the apoptotic cells were relatively negligible in control. As exhibited from the Fig. 9 MCF-7 cells when exposed to complex **1**, the early apoptosis cells increases to 11% at 2.5 μM to 23.2% at 5.0 μM concentrations. While, the percentage of late apoptosis cells reached to 9.5% and 7.8% in 2.5 μM and 5.0 μM , respectively. About 2.5% to 2.8% necrotic cells were also observed in both the concentrations used.

3.10. Effect of complex **1** in micronucleus formation

The genotoxic effects of complex **1** were studied on MCF-7 cells using cytokinesis-block micronucleus (CBMN) assay after 24 h of treatment. Micronuclei were scored in 1000 binucleated MCF-7 cells as micronucleated binucleated cells. Fig. 10 presents the photomicrographs of the MCF-7 cells in the CBMN assay including control and treatment group. The number of micronuclei scored per

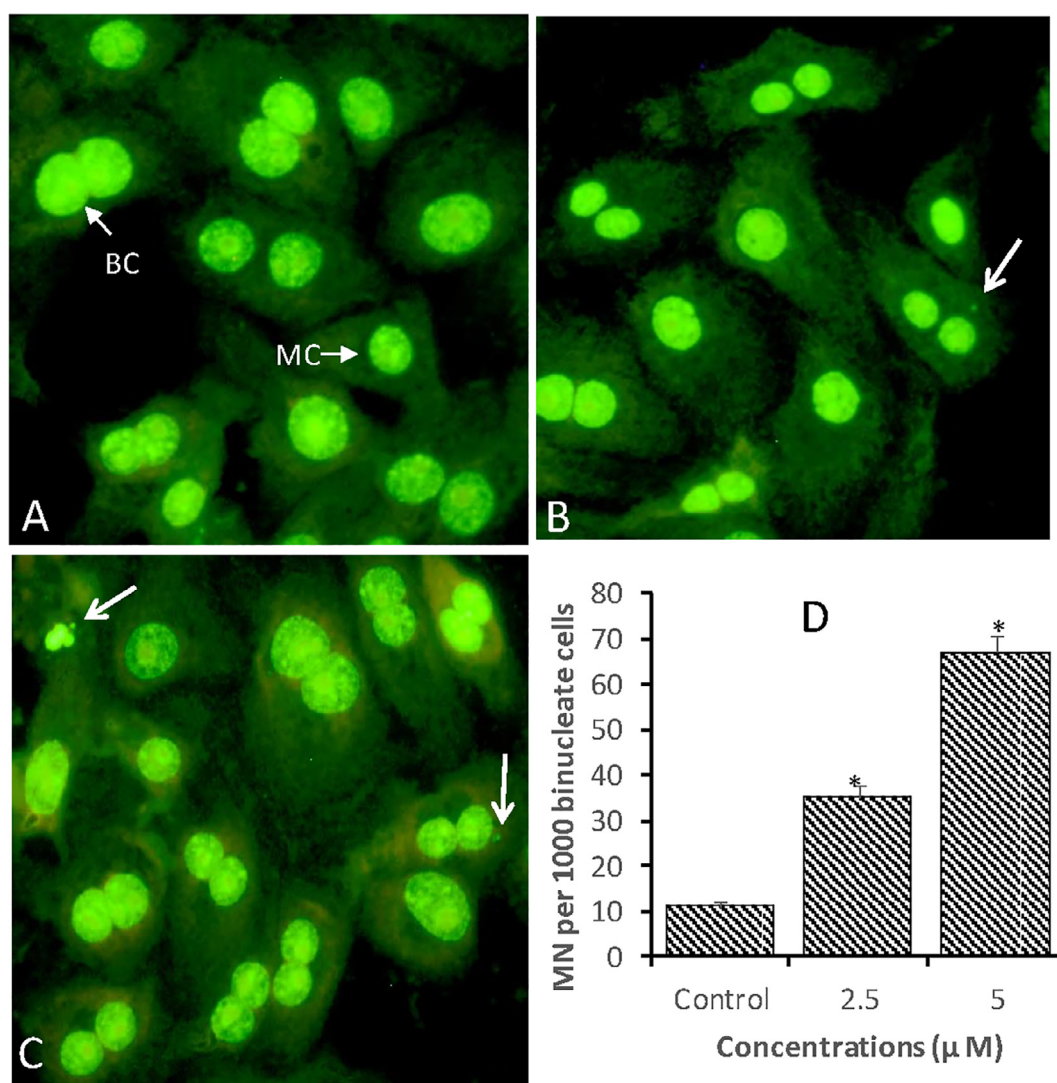


Fig. 10. Induction of micronuclei in MCF-7 human cancer cells observed by fluorescence microscopy. (A) Control (B) Complex **1** (2.5 μM) (C) Complex **1** (5.0 μM). BC: Binucleated cells; MC: Mononucleated cells; arrow head showing micronucleus. Magnification: 400X. (D) Quantitative estimation of micronucleus in 1000 binucleated cells in each experimental group. Data represented as $\pm\text{SE}$. * Significant ($p < 0.05$) compared with control.

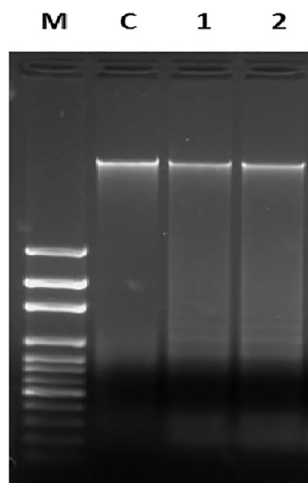


Fig. 11. Apoptotic effect of complex **1** in MCF-7 cells assessed by agarose gel electrophoresis. DNA ladder pattern was evident in all treated groups while control cells are showing a normal single band of DNA. Lanes: M- 100 bp DNA ladder marker, C- control, lane **1** – Complex **1** (2.5 μM), lane **2** – complex **1** (5.0 μM).

1000 binucleated MCF-7 cells increased significantly ($p < 0.05$) in a concentration-dependent manner. The data indicated that complex **1** was a potential inducer of MN causing a 3.1 and 6-fold increases in the frequency of MN at concentrations 2.5 μM and 5.0 μM , respectively.

3.11. Effect of complex **1** on DNA fragmentation in MCF-7 cells

Genomic DNA fragmentation resulting in a ladder formation on an agarose gel is a characteristic feature of apoptosis. For the analysis of the endonuclease cleavage products of apoptosis, DNA laddering is a valued technique. To elucidate whether complex **1** decreased cell survival by induction of DNA fragmentation, genomic DNA was extracted from MCF-7 cells following exposure to 2.5 and 5.0 μM for 24 h and analyzed by agarose gel electrophoresis. Fig. 11 (Lane 1 and 2) indicated multiple fragmentations of DNA shown as the DNA-laddering pattern in MCF-7 cells treated with complex **1** while in control DNA (Lane C) normal band of genomic DNA was observed. The formation of DNA ladder correlates with the early morphological signs of apoptosis which was also evident in the abnormal morphology of MCF-7 cells (Fig. 10B, C).

4. Conclusions

Herein, we have synthesized and characterized new $[\text{Cu}^{\text{II}}-\text{Na}^{\text{I}}]$ hetero-binuclear complex. DFT and Hirshfeld surface analysis revealed the various noncovalent atom-pairwise contacts responsible for the stabilization of Kagome-type 2D supramolecular assembly. The *in vitro* DNA binding experiments of complex **1** exhibited electrostatic binding with DNA by K_b value $(2.05 \pm 0.11) \times 10^4 \text{ M}^{-1}$. The gel electrophoresis assay demonstrated concentration-dependent cleavage pattern of pBR322 DNA with complex **1** and mechanistic exploration revealed that the ROS are responsible for cleavage activity. *In vitro* study with MCF-7 cells provides evidence that complex **1** has significant potential to induce cytotoxic activity and apoptosis. Its endonuclease activity was confirmed by nucleosomal fragment (50–200kbp) observed as DNA ladder. These results are in line with the DNA cleavage study where complex **1** exhibited potent cleavage activity. Altogether, the above findings suggest that complex **1** induced cell death through ROS generation, oxidative DNA damage, and DNA fragmentation.

Acknowledgements

The Authors are grateful to the Deanship of Scientific Research, King Saud University for funding through Vice Deanship of Scientific Research Chairs. We are thankful to the Department of Chemistry, AMU, India, UGC- DRS-II, DST-FIST, and DST- PURSE for instrumentation facility. Authors thankfully acknowledge IIT Roorkee for crystallography.

Appendix A. Supplementary data

Supplementary data associated with this article can be found, in the online version, at <https://doi.org/10.1016/j.ica.2018.04.036>.

References

- [1] J. Ferlay, I. Soerjomataram, M. Ervik, R. Dikshit, S. Eser, C. Mathers, et al., GLOBOCAN 2012 v1.0, Cancer Incidence and Mortality Worldwide: IARC Cancer Base No. 11 Lyon, France: International Agency for Research on Cancer, 2013.
- [2] B.W. Stewart, C.P. Wild, World cancer report 2014, Lyon: International Agency for Research on Cancer, 2014.
- [3] L. Dalla Via, S. Marciani Magno, O. Gia, A.M. Marini, F.D. Settimo, S. Salerno, C. La Motta, F. Simorini, S. Taliani, A. Lavecchia, C. Di Gio-vanni, G. Brancato, V. Barone, E. Novellino, *J. Med. Chem.* 52 (2009) 5429–5441.
- [4] (a) B. Rosenberg, *Interdisciplinary Sci. Rev.* 3 (1978) 134–147; (b) B. Rosenberg, L. VanCamp, J.E. Trosko, V.H. Mansour, *Nature* 222 (1969) 385–386; (c) P.C.A. Bruijninx, P.J. Sadler, *Curr. Opin. Chem. Biol.* 12 (2008) 197–206; (d) T.W. Hambley, *Dalton Trans.* (2007) 4929–4937; (e) C. Orvig, M.J. Abrams, *Chem. Rev.* 99 (1999) 2201–2204.
- [5] N.J. Wheate, S. Walker, G.E. Craig, R. Oun, *Dalton Trans.* 39 (2010) 8113–8127.
- [6] (a) E. Iniguez, A. Sánchez, M.A. Vasquez, A. Martínez, J. Olivas, A. Sattler, R.A. Sánchez-Delgado, R.A. Maldonado, *J. Biol. Inorg. Chem.* 18 (2013) 779–790; (b) L. Cai, G. Xu, C. Shi, D. Guo, X. Wang, J. Luo, *Biomaterials* 37 (2015) 456–468.
- [7] A.C. Komor, J.K. Barton, *Chem. Commun.* 49 (2013) 3617–3630.
- [8] C. Santini, M. Pellei, V. Gandin, M. Porchia, F. Tisato, C. Marzano, *Chem. Rev.* 114 (2014) 815–862.
- [9] (a) S.P. Fraser, I. Ozerlat-Gunduz, W.J. Brackenbury, E.M. Fitzgerald, T.M. Campbell, R.C. Coombes, M.B.A. Djamgoz, *Phil. Trans. R. Soc. B* 369 (2013) 20130105; (b) M. Li, Z. Xiong, *Int. J. Physiol. Pathophysiol. Pharmacol.* 3 (2011) 156–166; (c) A. Arcangeli, O. Crociani, E. Lastraioli, A. Masi, S. Pillozzi, A. Becchetti, *Curr. Med. Chem.* 16 (2009) 66–93; (d) N. Prevarskaya, R. Skryma, Y. Shuba, *Trends Mol. Med.* 16 (2010) 107–121.
- [10] J.V. McCarthy, T.G. Cotter, *Cell Death Differ.* 4 (1997) 756–770.
- [11] (a) S. Tabassum, M. Zaki, M. Afzal, F. Arjmand, *Dalton Trans.* 42 (2013) 10029–10041; (b) S. Tabassum, R.A. Khan, F. Arjmand, M. Aziz, A.S. Juvekar, S.M. Zingde, *Carbohydr. Res.* 346 (2011) 2886–2895; (c) S. Tabassum, R.A. Khan, F. Arjmand, A.S. Juvekar, S.M. Zingde, *Eur. J. Med. Chem.* 45 (2010) 4797–4806; (d) P. de Hoog, C. Boldron, P. Gamez, K. Sliedregt-Bol, I. Roland, M. Pitié, R. Kiss, B. Meunier, J. Reedijk, *J. Med. Chem.* 50 (2007) 3148–3152.
- [12] Y.Y. Karabach, A.M. Kirillov, M.F.C.G.D. da Silva, M.N. Kopylovich, A.J.L. Pombreiro, *Cryst. Growth Des.* 6 (2006) 2200–2203.
- [13] International Tables for X-Ray Crystallography, Kynoch Press vol. III (1952) 257–269.
- [14] SAINT, version 6.02; Bruker AXS: Madison, WI, 1999.
- [15] G.M. Sheldrick, SADABS, Empirical Absorption Correction Program, University of Göttingen, Göttingen, Germany, 1997.
- [16] XPREF, version 5.1; Siemens Industrial Automation Inc.: Madison, WI, 1995.
- [17] G.M. Sheldrick, SHELXTL Version 2016/6. <http://shelx.uniuc.gwdg.de/SHELXL/index.php>.
- [18] (a) F. Neese, *WIRES Comput. Mol. Sci.* 2 (2012) 73–78. (b) F. Neese, “Orca. An ab Initio, Density Functional, and Semiempirical Program Package version”, 2009.
- [19] C. Lee, W. Yang, R.G. Parr, *Phys. Rev. B* 37 (1988) 785–789.
- [20] (a) F. Weigend, R. Ahlrichs, *Phys. Chem. Chem. Phys.* 7 (2005) 3297–3305; (b) A. Schaefer, C. Huber, R. Ahlrichs, *J. Chem. Phys.* 100 (1994) 5829–5835; (c) A. Schaefer, H. Horn, R. Ahlrichs, *J. Chem. Phys.* 97 (1992) 2571–2577.
- [21] M.A. Spackman, D. Jayatilaka, *CrystEngComm.* 11 (2009) 19–32.
- [22] (a) O. Trott, A.J. Olson, *J. Comput. Chem.* 31 (2010) 455–461. (b) M.F. Sanner, *J. Mol. Graphics Mod.* 17 (1999) 57–61.
- [23] (a) Accelrys Software Inc., Discovery Studio Modeling Environment, Release 4.0, San Diego: Accelrys Software Inc., 2013. (b) The PyMOL Molecular Graphics System, Version 1.5.0.4 Schrödinger, LLC.
- [24] (a) J. Marmur, *J. Mol. Biol.* 3 (1961) 208–218; (b) M.E. Reicmann, S.A. Rice, C.A. Thomas, P. Doty, *J. Am. Chem. Soc.* 76 (1954) 3047–3053; (c) A. Wolfe, G.H. Shimer, T. Meehan, *Biochemistry* 26 (1987) 6392–6396; (d) J.R. Lakowicz, G. Weber, *Biochemistry* 12 (1973) 4161–4170.

- [25] (a) S. Tabassum, M. Afzal, H. Al-Lohedan, M. Zaki, R.A. Khan, M. Ahmad, *Inorg. Chim. Acta* 463 (2017) 142–155; (b) A. Folda, V. Scalcon, M. Ghazzali, M.H. Jaafar, R.A. Khan, A. Casini, A. Citta, A. Bindoli, M.P. Rigobello, K. Al-Farhan, A. Alsalmeh, J. Reedijk, *J. Inorganic Biochem.* 153 (2015) 346–354; (c) R.A. Khan, M. Usman, D. Rajakumar, P. Balaji, A. Alsalmeh, F. Arjmand, K. AlFarhan, M.A. Akbarsha, F. Marchetti, C. Pettinari, S. Tabassum, *Sci. Rep.* 7 (2017) 45229; (d) M. Usman, F. Arjmand, R.A. Khan, A. Alsalmeh, M. Ahmad, M.S. Bishwas, S. Tabassum, *Inorg. Chim. Acta* 473 (2018) 121–132; (e) M. Usman, F. Arjmand, R.A. Khan, A. Alsalmeh, M. Ahmad, S. Tabassum, *RSC Adv.* 7 (2017) 47920–47932.
- [26] P. Bhowmik, K. Harms, S. Chattopadhyay, *Polyhedron* 49 (2013) 113–120.
- [27] M. Usman, F. Arjmand, M. Ahmad, M.S. Khan, I. Ahmad, S. Tabassum, *Inorg. Chim. Acta* 453 (2016) 193–201.
- [28] (a) F. Arjmand, S. Sharma, M. Usman, B.M. Leu, M.Y. Hu, L. Toupet, D. Gosztola, S. Tabassum, *Phys. Chem. Chem. Phys.* 18 (2016) 17805–17809; (b) S. Yadav, I. Yousuf, M. Usman, M. Ahmad, F. Arjmand, S. Tabassum, *RSC Adv.* 5 (2015) 50673–50690.
- [29] P. Kumar, S. Gorai, M.K. Santra, B. Mondal, D. Manna, *Dalton Trans.* 41 (2012) 7573–7581.
- [30] M.S. Melvin, M.W. Calcutt, R.E. Noftle, R.A. Manderville, *Chem. Res. Toxicol.* 15 (2002) 742–748.
- [31] (a) C. Ravikumar, I.H. Joe, V.S. Jayakumar, *Chem. Phys. Lett.* 460 (2008) 552–558. (b) L. Padmaja, C. Ravikumar, D. Sajan, I.H. Joe, V.S. Jayakumar, G.R. Pettit, O.F. Nielsen, *J. Raman Spectrosc.* 40 (2009) 419–428. (c) W.M. Al-Asbahy, M. Usman, F. Arjmand, M. Shamsi, S. Tabassum *Inorg. Chim. Acta* 445 (2016) 167–178.
- [32] (a) D.F.V. Lewis, C. Ioannides, D.V. Parke, *Xenobiotica* 24 (1994) 401–408; (b) P. Thanikaivelan, V. Subramanian, J.R. Rao, B.U. Nair, *Chem. Phys. Lett.* 323 (2000) 59–70; (c) N. Kurita, K. Kobayashi, *Comput. Chem.* 24 (2000) 351–357.
- [33] B.K. Shoichet, S.L. McGovern, B. Wei, J.J. Irwin, *Curr. Opin. Chem. Biol.* 6 (2002) 439–446.